INORGANIC CHEMISTRY FRONTIERS

RESEARCH ARTICLE

View Article Online
View Journal | View Issue

Cite this: *Inorg. Chem. Front.*, 2023, **10**, 3955

Regulating the spin density of Co^{III} using boron-doped carbon dots for enhanced electrocatalytic nitrate reduction†

Jingjing Huang,‡[a] Jingkun Yu,‡[a] Xingmei Lu,[a] Yingying Wei,[a] Haoqiang Song,[a] Ang Cao,[b] Jinmeng Cai,*[a] Shuang-Quan Zang[a] and Siyu Lu*[a]

Received 9th May 2023,
Accepted 24th May 2023

DOI: 10.1039/d3qi00865g

rsc.li/frontiers-inorganic

Controlling the electron spin state on the catalyst surface can regulate the reaction activity, rate, and selectivity of surface reactions. However, there are still many challenges in exploring new strategies for electron spin regulation and mechanisms of the electron spin effect. Herein, we reported a method of using BCDs loading to change the electron spin density of magnetic Co_3O_4. Octahedral $Co^{3+}(O_h)$–O with a $t_{2g}^6e_g^0$ configuration transformed into $Co^{2+}(O_h)$–O with a $t_{2g}^5e_g^2$ configuration after BCDs loading showed excellent activity in the electrocatalytic nitrate reduction reaction, achieving a maximum NH_4^+ Faradaic efficiency of 94.6 ± 0.9% and high stability. Experimental results and theoretical calculations have found that high activity is attributed to the spin density regulation changing the rate-determining step and reducing the energy it needs to overcome. This work expands the spin density regulation methods and provides a new perspective for understanding the mechanisms of carbon dot materials in electrocatalytic reactions.

1. Introduction

In electrocatalytic reactions, changes in the electron spin can affect the chemical properties and reactivity of surface atoms or molecules on the catalyst, thereby affecting the rate and selectivity of the reaction.[1,2] For example, on the metal surface, the change of electron spin will affect the electron cloud density and binding energy of surface atoms, thus affecting the interaction and reactivity between atoms and reactants.[3] Secondly, the electron spin effect has an important impact on the reaction mechanism and reaction kinetics of catalysts. For example, in some catalytic reactions, electron spin can affect the generation and conversion of reaction intermediates, thereby affecting the rate and selectivity of the reaction.[4] At the same time, electron spin can also affect the stability and activation energy of the transition state of the reaction, thus affecting the dynamic characteristics and thermodynamic stability of the reaction.[5] Overall, there is a close relationship between electron spin and surface catalysis. By controlling the electron spin state on the catalyst surface, the reaction activity, rate, and selectivity of surface reactions can be regulated, providing new ideas and methods for preparing efficient and highly selective electrocatalysts.[6,7]

Researchers have proposed some electron spin regulation strategies, which can achieve high efficiency and selectivity of the catalyst by adjusting the state of electron spin in the catalyst.[8–10] One strategy is to regulate electron spin through external electromagnetic fields.[11] Researchers used external magnetic fields to regulate the state of electron spin in the catalyst, thereby controlling the catalytic efficiency and selectivity of the catalyst.[12] Another strategy is to achieve the regulation of electron spin through metal doping or alloying.[13] In this strategy, researchers doped other metal or semiconductor materials into the catalyst, thereby changing the state of electron spin in the catalyst and achieving the regulation of catalytic efficiency and selectivity.[14] These electron spin control strategies can effectively influence the properties of catalysts and improve the performance in applications.[15]

Herein, we reported the discovery of a new method for altering the electron spin density using non-metallic composites. Spin density modulation of Co-based spinel oxide (Co_3O_4) can be achieved by loading B-doped carbon dots (BCDs), that is octahedral $Co^{3+}(O_h)$–O with a $t_{2g}^6e_g^0$ electron configuration will be transformed into $Co^{2+}(O_h)$–O with a high spin $t_{2g}^5e_g^2$ configuration. The spin density-regulated BCDs/Co_3O_4/CC catalyst exhibited excellent activity in the electrocatalytic

[a]*Green Catalysis Center, and College of Chemistry, Zhengzhou University, Zhengzhou 450001, China. E-mail: caijinmeng@zzu.edu.cn, sylu2013@zzu.edu.cn*
[b]*Department of Physics, Technical University of Denmark, Kongens Lyngby 2800, Denmark*

†Electronic supplementary information (ESI) available. See DOI: https://doi.org/10.1039/d3qi00865g

‡These authors contributed equally to this work.

nitrate reduction reaction (NO_3RR) for ammonia synthesis,[16,17] achieving a maximum NH_4^+ Faradaic efficiency (FE) of 94.6 ± 0.9% at −1.3 V *vs.* SCE and high stability. This work demonstrates the feasibility of adjusting the spin density using BCDs, displaying the ability of carbon dots to change the catalytic performance by affecting metal spin states and providing new strategies for expanding the application and universality of carbon dot materials.

2. Results and discussion

2.1. Morphology and structural characterization

Before preparing the precursor catalyst, BCDs were synthesized from $C_6H_9BClNO_2$ using a hydrothermal method.[18] The detailed synthesis steps are described in the ESI.† To verify the successful preparation of BCDs, we performed transmission electron microscopy (TEM) characterization. The TEM morphological image in Fig. S1† shows that BCDs have a typical shape of quantum dots with an average diameter of around 4.1 nm. X-ray diffraction (XRD) measurements in Fig. S2† displays an obvious broad diffraction peak centered at 22.8°, which corresponds to the (100) crystal plane of graphitized carbon in BCDs.[19] Various related functional groups (C–C, C=C, C–N, B–O, and O–H) on the surface of BCDs were detected using Fourier transform infrared spectroscopy (FT-IR, Fig. S3†).[20] Additionally, X-ray photoelectron spectroscopy (XPS) was used to further understand the chemical structure and elemental composition of BCDs. As shown in Fig. S4,† the survey spectrum displayed that the BCDs were mainly composed of C, N, O and B. In the high resolution C 1s, N 1s, O 1s and B 1s spectra, the assignment of different functional groups corresponds well with the FT-IR results.[21] Based on the above results, we can confirm the successful preparation of BCDs.

The heterostructured BCDs/Co_3O_4/CC electrocatalyst was prepared by a two-step process as illustrated in Fig. 1a. First, a precursor catalyst BCDs/$Co(OH)_x$/CC supported on carbon cloth was synthesized through a hydrothermal method. The scanning electron microscopy (SEM) image in Fig. 1b shows the morphology of nanowires grown on carbon cloth fibers. Then, the as-prepared precursor catalyst was annealed at 450 °C for 6 h under an Ar atmosphere to obtain the BCDs/Co_3O_4/CC electrocatalyst. The SEM image of BCDs/Co_3O_4/CC in Fig. 1c still displays the morphology of nanowires without significant surface changes, which is similar to the changes in the control sample of Co_3O_4/CC (Fig. S5†). In order to further analyze the surface morphology and structure of BCDs/Co_3O_4/CC, we conducted TEM characterization. As shown in Fig. 1d, the primary structure of the nanowire morphology is nanoparticles with a diameter of 50–100 nm, which is connected one by one. Such a morphology is conducive to exposing more active sites than smooth nanowires. The high-resolution TEM (HRTEM) image shows that the sample has two distinct regions (Fig. 1e). One is the inner region with a highly crystalline lattice. The lattice spacing is 0.24 nm, corresponding to the (311) crystal plane of Co_3O_4.[22,23] The other region is a carbonized surface layer,

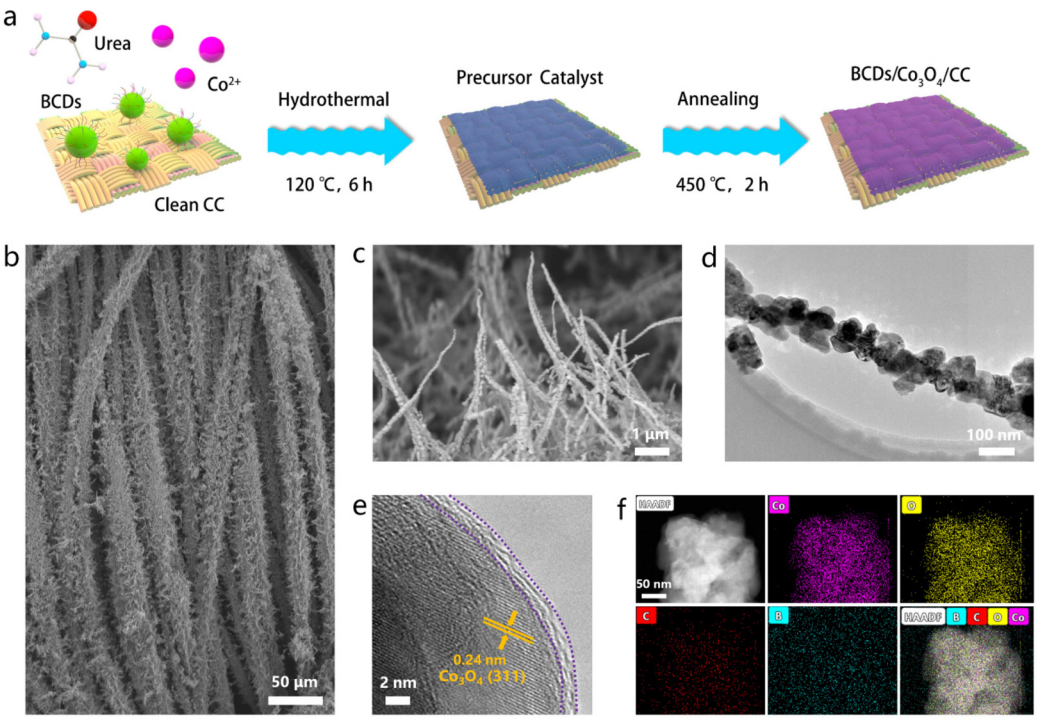

Fig. 1 Synthesis and characterization of BCDs/Co_3O_4/CC. (a) Schematic illustration of the synthesis of BCDs/Co_3O_4/CC. (b) SEM image of the precursor catalyst. (c–e) SEM, TEM and HRTEM images of BCDs/Co_3O_4/CC. (f) Element mapping images of BCDs/Co_3O_4/CC.

which is formed by the BCDs at high annealing temperatures. In addition, we analyzed the composition and distribution of elements in the sample, and the results shows that Co, O, C, and B were evenly distributed on the catalyst (Fig. 1f).

As a comparison, we also prepared Co_3O_4/CC using the same method without adding BCDs as a reactant. The XRD patterns of BCDs/Co_3O_4/CC, Co_3O_4/CC and CC are shown in Fig. S6a.† The diffraction peaks centered at 31.3, 36.9, 59.5 and 65.3° correspond to the Co_3O_4 phase (JCPDS No. 73-1701),[24] while the diffraction peak of graphitized carbon in the BCDs is covered by the broad diffraction peak of carbon cloth in the range of 20–30°. Raman tests were also used to analyze the structure of the three samples (Fig. S6b†). CC showed characteristic D and G peak signals at 1355 and 1601 cm^{-1}, respectively. After loading Co_3O_4 on CC, additional signals caused by Co_3O_4 appear in the region of 400–700 cm^{-1}.[25] Furthermore, XPS was used to analyze the element composition and surface chemical states of the catalyst. The survey spectrum of BCDs/Co_3O_4/CC shows the presence of Co, C, O, and B in the catalyst (Fig. S7†). The high-resolution Co 2p XPS spectra of BCDs/Co_3O_4/CC and Co_3O_4/CC in Fig. 2a show two main peaks (denoted by grey) at 781.6 and 797.1 eV, which could be ascribed to the Co $2p_{3/2}$ and Co $2p_{1/2}$ of Co^{2+} species.[26] The other two peaks denoted by red can be attributed to Co^{3+} species. In addition, the shake-up process of Co^{2+} species in high spin states leads to the appearance of two adjacent satellite peaks centered at 787.4 and 802.9 eV.[14] The proportion of Co^{3+} and Co^{2+} species in Co_3O_4/CC was calculated to be 62.1% and 37.9% (Fig. 2b), respectively, while this proportion changed to 34.4% and 65.6% in BCDs/Co_3O_4/CC (Fig. 2c). This result indicates an increased proportion of Co^{2+} species as a function of BCDs loading. In addition, the O 1s XPS spectra display peaks at 533.1, 530.9 and 529.3 eV due to C═O species, surface –OH groups and the lattice oxygen of Co–O in Co_3O_4, respectively (Fig. 2d).[27] Notably, the characteristic peak of B–O centered at 531.8 eV in BCDs/Co_3O_4/CC can be observed, further indicating the successful loading of BCDs. Moreover, the B 1s XPS spectrum of BCDs/Co_3O_4/CC also confirm the above results (Fig. 2e).[28]

On the basis of the above analysis, the valence electron configurations of Co with and without BCDs in Co_3O_4 are identified. Typically, as illustrated in Fig. 2f, Co_3O_4 has two types of Co–O species, that is, octahedral $Co^{3+}(O_h)$–O coordinated by six oxygen atoms (denoted by grey) and tetrahedral $Co^{2+}(T_d)$–O coordinated by four oxygen atoms (denoted by purple).[29] The theoretical proportion of Co^{2+} in Co_3O_4 inferred from the above crystal structure is 33.3%, which is close to the Co^{2+} proportion of 37.9% in Co_3O_4/CC. However, this proportion underwent a significant change to 65.6% after the loading of BCDs, indicating that the BCDs can act as an electron bridge to accelerate electron transfer from BCDs to $Co^{3+}(O_h)$, forming the $Co^{2+}(O_h)$ species. The valence electron configuration of $Co^{3+}(O_h)$ in Co_3O_4/CC is $t_{2g}^6e_g^0$, while $Co^{2+}(O_h)$ in BCDs/Co_3O_4/CC possesses a $t_{2g}^5e_g^2$ configuration with three unpaired electrons, as illustrated in Fig. 2g.[30] Specifically, the π-symmetry t_{2g} of $Co^{3+}(O_h)$ is fully occupied, which would result in electron repulsion between Co^{3+} and the reactant.[7] As for the unpaired

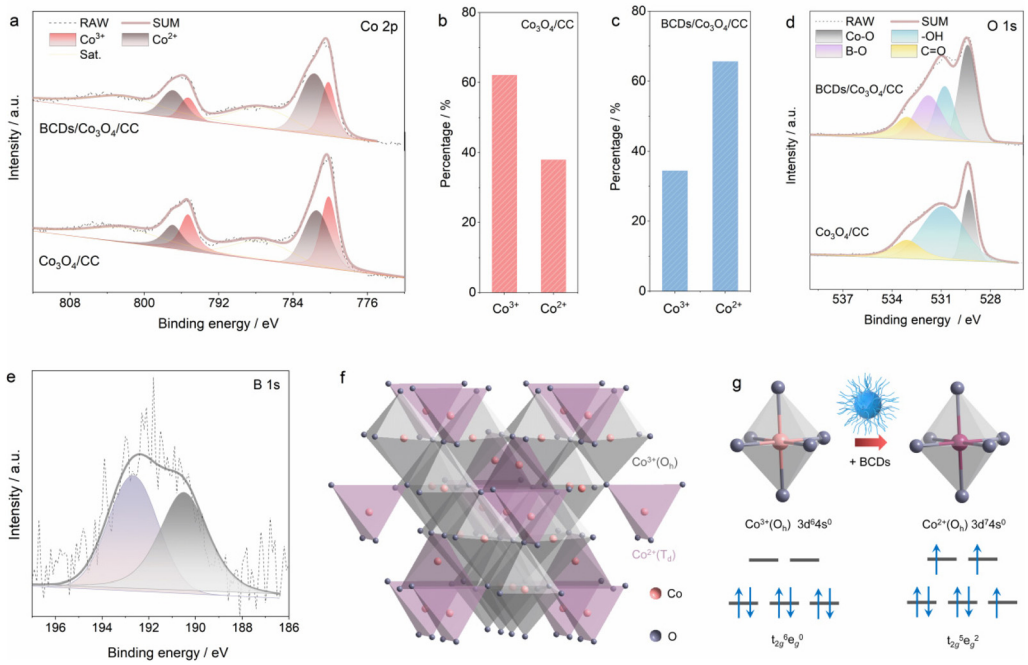

Fig. 2 Surface property characterization. (a) XPS spectra of the Co 2p region of the Co_3O_4/CC and BCDs/Co_3O_4/CC. (b and c) Calculated ratio of Co^{3+} and Co^{2+} in Co_3O_4/CC and BCDs/Co_3O_4/CC, respectively. (d) O 1s region of Co_3O_4/CC and BCDs/Co_3O_4/CC. (e) B 1s region of BCDs/Co_3O_4/CC. (f) Crystal structure of Co_3O_4. (g) Scheme of the valence electron configurations and spin states of octahedral Co influenced by the BCDs.

electron in $Co^{2+}(O_h)$, π-donation *via* O–Co–O would be strengthened by BCDs loading. In summary, the BCDs can alter the electronic structure of Co_3O_4 and regulate the spin state of $Co^{3+}(O_h)$ to active $Co^{2+}(O_h)$ species.

2.2. Electrocatalytic performances

The spin density-regulated BCDs/Co_3O_4/CC electrocatalyst was applied for nitrate reduction reaction measurements. We used a typical H-type three electrode reactor for performance testing, where 50 mL of 0.5 M K_2SO_4 and 0.5 M K_2SO_4 + 200 ppm NO_3^-–N electrolyte were added to the anode and cathode chambers, respectively.[31–33] As shown in Fig. 3a, there is no significant difference between the linear sweep voltammetry (LSV) curves of CC before and after the addition of nitrate, which indicates that the influence and contribution of the substrate material to the reaction performance are basically zero. As for the BCDs/Co_3O_4/CC and Co_3O_4/CC electrocatalysts, the current density of the LSV curves significantly increased after the adding of nitrate. Meanwhile, BCDs/Co_3O_4/CC shows a higher current density compared to Co_3O_4/CC. Additionally, the catalytic performance of BCDs/CC was also tested (Fig. S8†), and the low current density indicated that the activity of single-component BCDs was weak in electrocatalytic nitrate-to-ammonia conversion. The above results revealed that nitrate participates in the reaction and the spin density of Co_3O_4 regulated by BCDs effectively improves the performance of the reaction.[34] Then, we tested nitrate reduction at fixed potentials, and measured the concentration of each ion in the electrolyte after the reaction using ion chromatography (IC, Fig. S9–S11†).[35,36] As displayed in Fig. 3b, with the increase of applied potentials, the FE of NH_4^+ exhibits a volcanic trend of first increasing and then decreasing, and can reach a maximum FE of 94.6 ± 0.9% at −1.3 V *vs.* SCE. Furthermore, the NH_4^+ generation rate gradually increases with the lowering of potentials, reaching 193.3 μmol h^{-1} cm^{-2} at −1.4 V *vs.* SCE (Fig. 3c).

In order to determine whether the spin density-regulated BCDs/Co_3O_4/CC electrocatalyst can work effectively for a long time, we conducted stability tests at −1.3 V *vs.* SCE.[37] As shown in Fig. 3d and e, under four consecutive cyclic tests, the FE of NH_4^+ and the current density remained basically unchanged, indicating that the BCDs/Co_3O_4/CC electrocatalyst can maintain good stability during the electrocatalytic process. In addition, to confirm that the ammonia generated during the reaction process comes from the reduction of nitrate, we used isotope labeling experiments to detect the source of nitrogen in the ammonia.[38–40] Under the same reaction conditions, $^{15}NO_3^-$ was used to replace the original $^{14}NO_3^-$ as the reactant, and the ammonia was generated by a continuous reaction at −1.3 V *vs.* SCE. When $^{14}NO_3^-$ was used, the ^1H nuclear magnetic resonance (NMR, 600 MHz) spectrum showed a typical triple peaks for $^{14}NH_4^+$. When $^{15}NO_3^-$ was used, the ^1H NMR spectrum displayed a double peaks for $^{15}NH_4^+$ (Fig. 3f).[41] Therefore, we determined that the NH_4^+ obtained by the reaction was reduced from the added NO_3^-, excluding the interference of the reaction system or other nitrogen-containing compounds.

2.3. Density functional theory (DFT) calculations

DFT calculations were utilized to further understand the activity of BCDs/Co_3O_4/CC for the electrocatalytic NO_3RR.[42] First, we calculated the direction and amount of charge transfer on the composite catalyst using Bader charge analysis. As shown in Fig. 4a, the B atoms will transfer 1.76 and 1.82 elec-

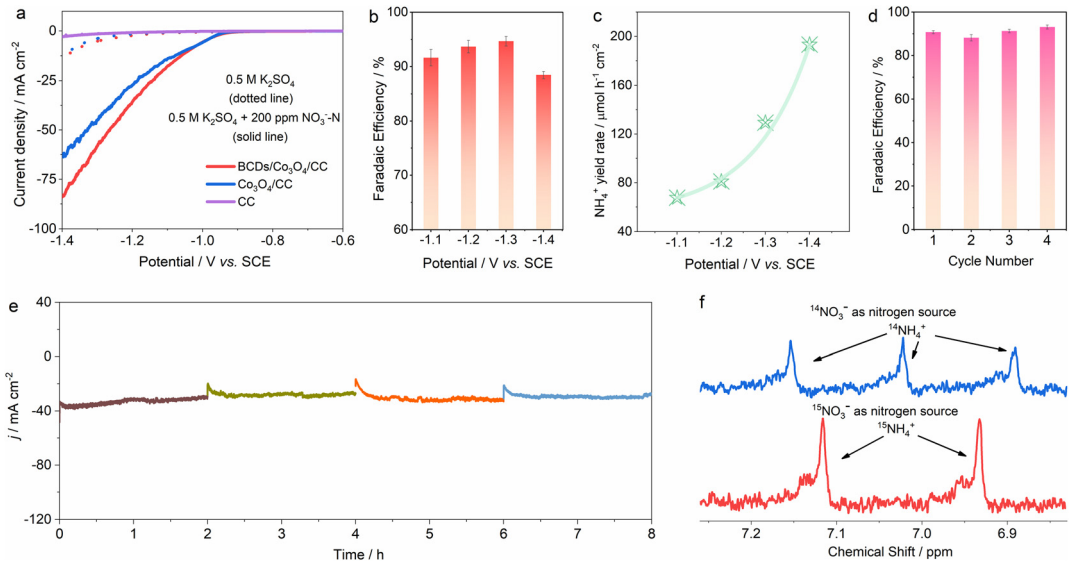

Fig. 3 Electrocatalytic nitrate reduction performances. (a) LSV curves of BCDs/Co_3O_4/CC, Co_3O_4/CC, and CC. (b and c) NH_4^+ FEs and NH_4^+ yield rates of BCDs/Co_3O_4/CC at different applied potentials. (d and e) Stability test (repeated for four times) and the corresponding NH_4^+ FEs of BCDs/Co_3O_4/CC at a potential of −1.3 V *vs.* SCE. (f) ^1H NMR spectra of electrocatalytic nitrate-to-ammonia conversion on BCDs/Co_3O_4/CC at −1.3 V *vs.* SCE by using $^{14}NO_3^-$ and $^{15}NO_3^-$ as the nitrogen source.

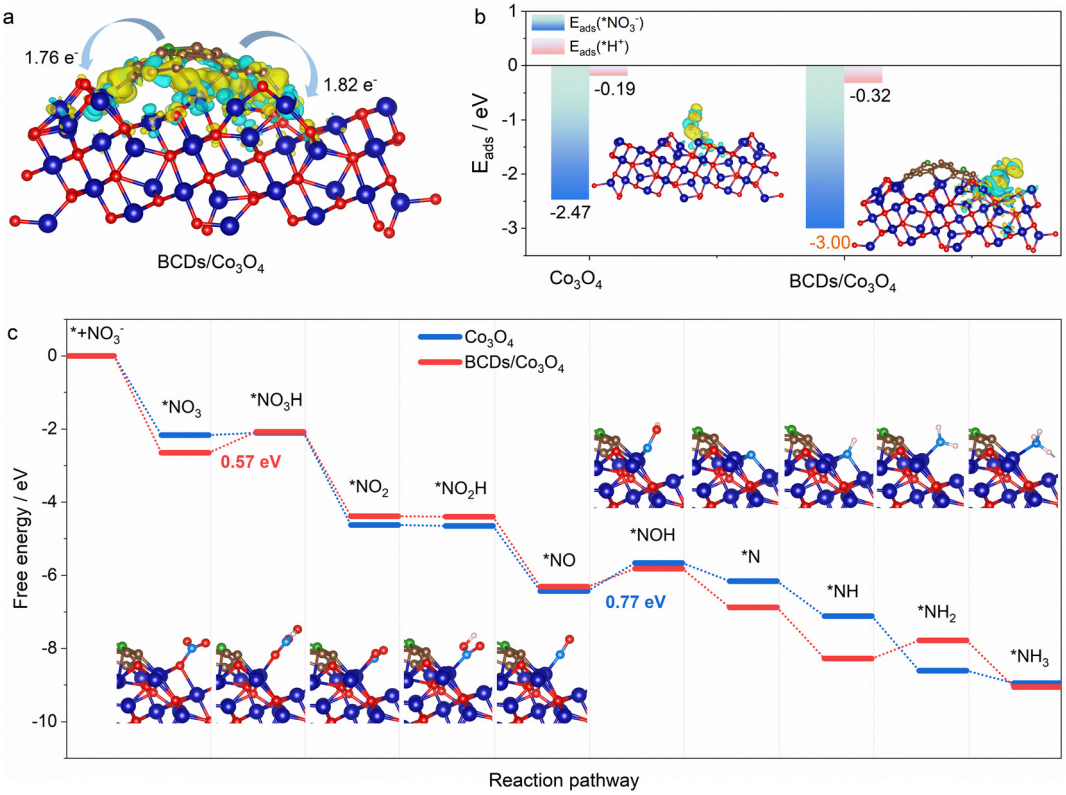

Fig. 4 Mechanism investigation. (a) Charge density difference and Bader charge of BCDs/Co_3O_4. The yellow and blue electronic clouds indicate charge accumulation and depletion. (b) The adsorption energy for NO_3^- and H^+ on Co_3O_4 and BCDs/Co_3O_4. Insets show the charge-density difference for NO_3^- adsorption. (c) Free-energy diagrams of nitrate reduction to ammonia on the surface of Co_3O_4 and BCDs/Co_3O_4. Insets show the optimized configurations for adsorbates on the surface of BCDs/Co_3O_4.

trons to the adjacent metal Co on the BCDs/Co_3O_4/CC catalyst. Therefore, BCDs can serve as a bridge for electron transfer from B atoms to the octahedral $Co^{3+}(O_h)$, forming active high-spin $Co^{2+}(O_h)$ with a $t_{2g}^5e_g^2$ configuration.[43] Furthermore, thecompetitive hydrogen evolution reaction is the main reason for the decrease in the FE of ammonia in the electrocatalytic NO_3RR.[44] Therefore, we also calculated the adsorption energy for the interaction between nitrate and H^+ on the catalyst surface. As displayed in Fig. 4b, the adsorption energies for nitrate on BCDs/Co_3O_4/CC and Co_3O_4/CC are 3.00 and 2.47 eV, respectively, indicating that BCDs/Co_3O_4/CC has a stronger adsorption effect on nitrate. This is beneficial for the adsorption and occupation of nitrate on the catalyst surface and improves the catalytic reaction performance. Meanwhile, the adsorption energies for H^+ on BCDs/Co_3O_4/CC and Co_3O_4/CC were 0.32 and 0.19 eV, respectively, much lower than the adsorption energies of nitrate. This indicates that the hydrogen evolution reaction can be effectively suppressed on the surfaces of these two catalysts, which is consistent with the high FE of the test results.

Based on our experimental testing and computational findings, we have deduced a possible reaction pathway for nitrate reduction to generate ammonia (Fig. 4c).[45] The most favorable pathway is as follows:

$$NO_3^- \xrightarrow{H^+} HNO_3^* \xrightarrow{H^+ + e^-} NO_2^* \xrightarrow{H^+ + e^-}$$
$$NOOH^* \xrightarrow{H^+ + e^-} NO^* \xrightarrow{H^+ + e^-} NOH^* \xrightarrow{H^+ + e^-}$$
$$N^* \xrightarrow{H^+ + e^-} NH^* \xrightarrow{H^+ + e^-} NH_2^* \xrightarrow{H^+ + e^-} NH_3^*.$$

For the Co_3O_4/CC catalyst without spin regulation, the rate-determining step of the reaction is the conversion of NO* to NOH*, while for the BCDs/Co_3O_4/CC catalyst with spin regulation, the rate-determining step of the reaction is the hydrogenation of NO_3*. Therefore, for BCDs/Co_3O_4/CC, the rate-determining step has changed and the energy to be overcome in this step has also decreased, resulting in a significantly improved electrocatalytic performance.

3. Conclusion

In summary, we report a method of using BCDs loading to alter the electron spin density of magnetic metal oxides. Octahedral $Co^{3+}(O_h)$–O with a $t_{2g}^6e_g^0$ electronic configuration transforms into octahedral $Co^{2+}(O_h)$–O with a $t_{2g}^5e_g^2$ configuration after BCDs loading. The BCDs/Co_3O_4/CC catalyst with

spin density regulation showed excellent activity in the electrocatalytic NO_3RR for ammonia synthesis, achieving a maximum NH_4^+ FE of 94.6 ± 0.9% and high stability at −1.3 V *vs.* SCE. The high activity is attributed to the spin density regulation changing the rate-determining step and reducing the energy it needs to overcome. This work expands the methods of spin density regulation and provides a new perspective on the mechanism of carbon dot materials in catalytic reactions.

Author contributions

Conceptualization: J.C. and S.L.; methodology: J.Y. and A.C.; investigation: J.H., X.L., H.S., and Y.W.; writing – original draft: J.H. and X.L.; writing – review and editing: J.C., S.Q.Z., and S. L.; funding acquisition: J.C., S.L., and S.Q.Z.; supervision: S.L.

Conflicts of interest

The authors declare no competing financial interest.

Acknowledgements

This work was supported by the National Natural Science Foundation of China (No. 22205213), the China Postdoctoral Science Foundation (2020M682332, 2021T140614), the Natural Science Foundation of Henan Province (222300420287), and the Henan Postdoctoral Foundation (202003015).

References

1 J. Suntivich, K. J. May, H. A. Gasteiger, J. B. Goodenough and Y. Shao-Horn, A Perovskite Oxide Optimized for Oxygen Evolution Catalysis from Molecular Orbital Principles, *Science*, 2011, **334**, 1383–1385.
2 A. L. Buchachenko and V. L. Berdinsky, Electron Spin Catalysis, *Chem. Rev.*, 2002, **102**, 603–612.
3 J. Lv, P. Liu, R. Li, L. Wang, K. Zhang, P. Zhou, X. Huang and G. Wang, Constructing accelerated charge transfer channels along V-Co-Fe via introduction of V into CoFe-layered double hydroxides for overall water splitting, *Appl. Catal., B*, 2021, **298**, 120587.
4 A. Cao and J. K. Nørskov, Spin Effects in Chemisorption and Catalysis, *ACS Catal.*, 2023, **13**, 3456–3462.
5 C. Y. Zhang, C. Zhang, G. W. Sun, J. L. Pan, L. Gong, G. Z. Sun, J. J. Biendicho, L. Balcells, X. L. Fan, J. R. Morante, J. Y. Zhou and A. Cabot, Spin Effect to Promote Reaction Kinetics and Overall Performance of Lithium-Sulfur Batteries under External Magnetic Field, *Angew. Chem., Int. Ed.*, 2022, **61**, e202211570.
6 J. Xu, X. Zhong, X. Wu, Y. Wang and S. Feng, Optimizing the electronic spin state and delocalized electron of $NiCo_2(OH)_x$/MXene composite by interface engineering and plasma boosting oxygen evolution reaction, *J. Energy Chem.*, 2022, **71**, 129–140.
7 Z. Sun, L. Lin, J. He, D. Ding, T. Wang, J. Li, M. Li, Y. Liu, Y. Li, M. Yuan, B. Huang, H. Li and G. Sun, Regulating the Spin State of Fe^{III} Enhances the Magnetic Effect of the Molecular Catalysis Mechanism, *J. Am. Chem. Soc.*, 2022, **144**, 8204–8213.
8 A. Cao, V. J. Bukas, V. Shadravan, Z. Wang, H. Li, J. Kibsgaard, I. Chorkendorff and J. K. Nørskov, A spin promotion effect in catalytic ammonia synthesis, *Nat. Commun.*, 2022, **13**, 2382.
9 Y. C. Liang, M. Lihter and M. Lingenfelder, Spin-Control in Electrocatalysis for Clean Energy, *Isr. J. Chem.*, 2022, **62**, e202200052.
10 Z. Li, R. Ma, Q. Ju, Q. Liu, L. Liu, Y. Zhu, M. Yang and J. Wang, Spin engineering of single-site metal catalysts, *Innovation*, 2022, **3**, 100268.
11 S. Luo, K. Elouarzaki and Z. J. Xu, Electrochemistry in Magnetic Fields, *Angew. Chem., Int. Ed.*, 2022, **61**, e202203564.
12 X. Ren, T. Wu, Y. Sun, Y. Li, G. Xian, X. Liu, C. Shen, J. Gracia, H.-J. Gao, H. Yang and Z. J. Xu, Spin-polarized oxygen evolution reaction under magnetic field, *Nat. Commun.*, 2021, **12**, 2608.
13 C.-C. Lin, T.-R. Liu, S.-R. Lin, K. M. Boopathi, C.-H. Chiang, W.-Y. Tzeng, W.-H. C. Chien, H.-S. Hsu, C.-W. Luo, H.-Y. Tsai, H.-A. Chen, P.-C. Kuo, J. Shiue, J.-W. Chiou, W.-F. Pong, C.-C. Chen and C.-W. Chen, Spin-Polarized Photocatalytic CO_2 Reduction of Mn-Doped Perovskite Nanoplates, *J. Am. Chem. Soc.*, 2022, **144**, 15718–15726.
14 Z. Li, Z. Wang, S. Xi, X. Zhao, T. Sun, J. Li, W. Yu, H. Xu, T. S. Herng, X. Hai, P. Lyu, M. Zhao, S. J. Pennycook, J. Ding, H. Xiao and J. Lu, Tuning the Spin Density of Cobalt Single-Atom Catalysts for Efficient Oxygen Evolution, *ACS Nano*, 2021, **15**, 7105–7113.
15 Y. Sun, S. Sun, H. Yang, S. Xi, J. Gracia and Z. J. Xu, Spin-Related Electron Transfer and Orbital Interactions in Oxygen Electrocatalysis, *Adv. Mater.*, 2020, **32**, 2003297.
16 X. Lu, H. Song, J. Cai and S. Lu, Recent development of electrochemical nitrate reduction to ammonia: A mini review, *Electrochem. Commun.*, 2021, **129**, 107094.
17 H. Wang, J. Huang, J. Cai, Y. Wei, A. Cao, B. Liu and S. Lu, In Situ/Operando Methods for Understanding Electrocatalytic Nitrate Reduction Reaction, *Small Methods*, 2023, 2300169.
18 X. Lu, J. Yu, J. Cai, Q. Zhang, S. Yang, L. Gu, G. I. N. Waterhouse, S.-Q. Zang, B. Yang and S. Lu, Exclusive nitrate to ammonia conversion via boron-doped carbon dots induced surface Lewis acid sites, *Cell Rep. Phys. Sci.*, 2022, **3**, 100961.
19 X. Miao, D. Qu, D. Yang, B. Nie, Y. Zhao, H. Fan and Z. Sun, Synthesis of Carbon Dots with Multiple Color Emission by Controlled Graphitization and Surface Functionalization, *Adv. Mater.*, 2018, **30**, 1704740.
20 Q. Zhang, R. Wang, B. Feng, X. Zhong and K. Ostrikov, Photoluminescence mechanism of carbon dots: triggering

high-color-purity red fluorescence emission through edge amino protonation, *Nat. Commun.*, 2021, **12**, 6856.

21 Y.-X. Wang, M. Rinawati, W.-H. Huang, Y.-S. Cheng, P.-H. Lin, K.-J. Chen, L.-Y. Chang, K.-C. Ho, W.-N. Su and M.-H. Yeh, Surface-engineered N-doped carbon nanotubes with B-doped graphene quantum dots: Strategies to develop highly-efficient noble metal-free electrocatalyst for online-monitoring dissolved oxygen biosensor, *Carbon*, 2022, **186**, 406–415.

22 Y. Wang, C. Zhu, G. Zuo, Y. Guo, W. Xiao, Y. Dai, J. Kong, X. Xu, Y. Zhou, A. Xie, C. Sun and Q. Xian, 0D/2D Co_3O_4/TiO_2 Z-Scheme heterojunction for boosted photocatalytic degradation and mechanism investigation, *Appl. Catal., B*, 2020, **278**, 119298.

23 L. Lai, J. Zhu, Z. Li, D. Y. W. Yu, S. Jiang, X. Cai, Q. Yan, Y. M. Lam, Z. Shen and J. Lin, Co_3O_4/nitrogen modified graphene electrode as Li-ion battery anode with high reversible capacity and improved initial cycle performance, *Nano Energy*, 2014, **3**, 134–143.

24 S. H. Hsu, S. F. Hung, H. Y. Wang, F. X. Xiao, L. P. Zhang, H. B. Yang, H. M. Chen, J. M. Lee and B. Liu, Tuning the Electronic Spin State of Catalysts by Strain Control for Highly Efficient Water Electrolysis, *Small Methods*, 2018, **2**, 1800001.

25 M. Rashad, M. Rusing, G. Berth, K. Lischka and A. Pawlis, CuO and Co_3O_4 Nanoparticles: Synthesis, Characterizations, and Raman Spectroscopy, *J. Nanomater.*, 2013, 82.

26 W. Chu, P. A. Chernavskii, L. Gengembre, G. A. Pankina, P. Fongarland and A. Y. Khodakov, Cobalt species in promoted cobalt alumina-supported Fischer–Tropsch catalysts, *J. Catal.*, 2007, **252**, 215–230.

27 H. Wu, M. Wu, B. Wang, X. Yong, Y. Liu, B. Li, B. Liu and S. Lu, Interface electron collaborative migration of Co–Co_3O_4/carbon dots: Boosting the hydrolytic dehydrogenation of ammonia borane, *J. Energy Chem.*, 2020, **48**, 43–53.

28 Y.-X. Wang, M. Rinawati, J.-D. Zhan, K.-Y. Lin, C.-J. Huang, K.-J. Chen, H. Mizuguchi, J.-C. Jiang, B.-J. Hwang and M.-H. Yeh, Boron-Doped Graphene Quantum Dots Anchored to Carbon Nanotubes as Noble Metal-Free Electrocatalysts of Uric Acid for a Wearable Sweat Sensor, *ACS Appl. Nano Mater.*, 2022, **5**, 11100–11110.

29 Z. Xiao, Y. Wang, Y.-C. Huang, Z. Wei, C.-L. Dong, J. Ma, S. Shen, Y. Li and S. Wang, Filling the oxygen vacancies in Co_3O_4 with phosphorus: an ultra-efficient electrocatalyst for overall water splitting, *Energy Environ. Sci.*, 2017, **10**, 2563–2569.

30 C. Mu, J. Mao, J. Guo, Q. Guo, Z. Li, W. Qin, Z. Hu, K. Davey, T. Ling and S. Z. Qiao, Rational Design of Spinel Cobalt Vanadate Oxide Co_2VO_4 for Superior Electrocatalysis, *Adv. Mater.*, 2020, **32**, 1907168.

31 D. Qi, F. Lv, T. Wei, M. Jin, G. Meng, S. Zhang, Q. Liu, W. Liu, D. Ma, M. S. Hamdy, J. Luo and X. Liu, High-efficiency electrocatalytic NO reduction to NH_3 by nanoporous VN, *Nano Res. Energy*, 2022, **1**, e9120022.

32 J. Cai, Y. Wei, A. Cao, J. Huang, Z. Jiang, S. Lu and S.-Q. Zang, Electrocatalytic nitrate-to-ammonia conversion with ~100% Faradaic efficiency via single-atom alloying, *Appl. Catal., B*, 2022, **316**, 121683.

33 Y. M. Wang, J. Cai, Q. Y. Wang, Y. Li, Z. Han, S. Li, C. H. Gong, S. Wang, S. Q. Zang and T. C. W. Mak, Electropolymerization of metal clusters establishing a versatile platform for enhanced catalysis performance, *Angew. Chem., Int. Ed.*, 2022, **61**, e202114538.

34 Y. Wang, W. Zhou, R. Jia, Y. Yu and B. Zhang, Unveiling the activity origin of a copper–based electrocatalyst for selective nitrate reduction to ammonia, *Angew. Chem., Int. Ed.*, 2020, **59**, 5350–5354.

35 Y. Zhao, F. Wu, Y. Miao, C. Zhou, N. Xu, R. Shi, L. Z. Wu, J. Tang and T. Zhang, Revealing Ammonia Quantification Minefield in Photo/Electrocatalysis, *Angew. Chem., Int. Ed.*, 2021, **60**, 21728–21731.

36 Y. Zhao, R. Shi, X. Bian, C. Zhou, Y. Zhao, S. Zhang, F. Wu, G. I. N. Waterhouse, L. Z. Wu, C. H. Tung and T. Zhang, Ammonia Detection Methods in Photocatalytic and Electrocatalytic Experiments: How to Improve the Reliability of NH_3 Production Rates?, *Adv. Sci.*, 2019, **6**, 1802109.

37 F.-Y. Chen, Z.-Y. Wu, S. Gupta, D. J. Rivera, S. V. Lambeets, S. Pecaut, J. Y. T. Kim, P. Zhu, Y. Z. Finfrock, D. M. Meira, G. King, G. Gao, W. Xu, D. A. Cullen, H. Zhou, Y. Han, D. E. Perea, C. L. Muhich and H. Wang, Efficient conversion of low-concentration nitrate sources into ammonia on a Ru-dispersed Cu nanowire electrocatalyst, *Nat. Nanotechnol.*, 2022, **17**, 759–767.

38 Y. Zhang, X. Chen, W. Wang, L. Yin and J. C. Crittenden, Electrocatalytic nitrate reduction to ammonia on defective $Au_1Cu(111)$ single-atom alloys, *Appl. Catal., B*, 2022, **310**, 121346.

39 Q. Liu, L. Xie, J. Liang, Y. Ren, Y. Wang, L. Zhang, L. Yue, T. Li, Y. Luo, N. Li, B. Tang, Y. Liu, S. Gao, A. A. Alshehri, I. Shakir, P. O. Agboola, Q. Kong, Q. Wang, D. Ma and X. Sun, Ambient Ammonia Synthesis via Electrochemical Reduction of Nitrate Enabled by $NiCo_2O_4$ Nanowire Array, *Small*, 2022, **18**, 2106961.

40 H. Liu, X. Lang, C. Zhu, J. Timoshenko, M. Ruscher, L. Bai, N. Guijarro, H. Yin, Y. Peng, J. Li, Z. Liu, W. Wang, B. R. Cuenya and J. Luo, Efficient Electrochemical Nitrate Reduction to Ammonia with Copper-Supported Rhodium Cluster and Single-Atom Catalysts, *Angew. Chem., Int. Ed.*, 2022, **61**, e202202556.

41 Q. Gao, B. Yao, H. S. Pillai, W. Zang, X. Han, Y. Liu, S.-W. Yu, Z. Yan, B. Min, S. Zhang, H. Zhou, L. Ma, H. Xin, Q. He and H. Zhu, Synthesis of core/shell nanocrystals with ordered intermetallic single-atom alloy layers for nitrate electroreduction to ammonia, *Nat. Synth.*, 2023, DOI: **10.1038/s44160-023-00258-x**.

42 H. Niu, Z. Zhang, X. Wang, X. Wan, C. Shao and Y. Guo, Theoretical Insights into the Mechanism of Selective Nitrate–to–Ammonia Electroreduction on Single–Atom Catalysts, *Adv. Funct. Mater.*, 2020, **31**, 2008533.

43 R. R. Chen, Y. Sun, S. J. H. Ong, S. Xi, Y. Du, C. Liu, O. Lev and Z. J. Xu, Antiferromagnetic Inverse Spinel Oxide $LiCoVO_4$ with Spin-Polarized Channels for Water Oxidation, *Adv. Mater.*, 2020, **32**, 1907976.
44 Y. Wang, A. Xu, Z. Wang, L. Huang, J. Li, F. Li, J. Wicks, M. Luo, D.-H. Nam, C.-S. Tan, Y. Ding, J. Wu, Y. Lum, C.-T. Dinh, D. Sinton, G. Zheng and E. H. Sargent, Enhanced nitrate-to-ammonia activity on copper–nickel alloys via tuning of intermediate adsorption, *J. Am. Chem. Soc.*, 2020, **142**, 5702–5708.
45 J. Cai, J. Huang, A. Cao, Y. Wei, H. Wang, X. Li, Z. Jiang, G. I. N. Waterhouse, S. Lu and S.-Q. Zang, Interfacial hydrogen bonding-involved electrocatalytic ammonia synthesis on OH-terminated MXene, *Appl. Catal., B*, 2023, **328**, 122473.